Thermodynamic and liquid profiling during the 2010 Winter Olympics

R. Ware [a,b,c,*], D. Cimini [d,e], E. Campos [f], G. Giuliani [g], S. Albers [h,i], M. Nelson [a], S.E. Koch [j], P. Joe [k], S. Cober [k]

[a] Radiometrics, 4909 Nautilus Court North, Boulder, CO, USA
[b] National Center for Atmospheric Research, Boulder, CO, USA
[c] Cooperative Institute for Research in the Environmental Sciences, Boulder, CO, USA
[d] Center of Excellence for Severe Weather Forecast, L'Aquila, Italy
[e] Institute of Methodologies for Environmental Analysis, Tito Scalo, Italy
[f] Argonne National Laboratory, Argonne, IL, USA
[g] Abdus Salam International Centre for Theoretical Physics, Strada Costiera, Trieste, Italy
[h] Cooperative Institute for Research in the Atmosphere, Ft. Collins, CO, USA
[i] Earth System Research Laboratory, Boulder, CO, USA
[j] NOAA National Severe Storms Laboratory, Norman, OK, USA
[k] Environment Canada, Meteorological Research Division, Toronto, Canada

ARTICLE INFO

ABSTRACT

Tropospheric observations by a microwave profiling radiometer and six-hour radiosondes were obtained during the Alpine Venue of the 2010 Winter Olympic Games at Whistler, British Columbia, by Environment Canada. The radiometer provided continuous temperature, humidity and liquid (water) profiles during all weather conditions including rain, sleet and snow. Gridded analysis was provided by the U.S. National Oceanic and Atmospheric Administration. We compare more than two weeks of radiometer neural network and radiosonde temperature and humidity soundings including clear and precipitating conditions. Corresponding radiometer liquid and radiosonde wind soundings are shown. Close correlation is evident between radiometer and radiosonde temperature and humidity profiles up to 10 km height and among southwest winds, liquid water and upper level thermodynamics, consistent with up-valley advection and condensation of moist maritime air. We compare brightness temperatures observed by the radiometer and forward-modeled from radiosonde and gridded analysis. Radiosonde-equivalent observation accuracy is demonstrated for radiometer neural network temperature and humidity retrievals up to 800 m height and for variational retrievals that combine radiometer and gridded analysis up to 10 km height.

1. Introduction

Tropospheric thermodynamic (temperature and humidity) and liquid profiles are continuously generated by ground-based microwave radiometer profilers (MPs) operated by national and regional meteorological services. MP distribution is similar to that of radiosondes in Europe, China and Korea and is emerging elsewhere (India, Thailand, the United States, Japan and Columbia). Although instrumented balloon launches (radiosondes) remain the de facto standard

* Corresponding author at: Radiometrics, 4909 Nautilus Court North, Boulder, CO 80302, USA. Tel.: +1 303 449 9192; fax: +1 303 786 9343.
E-mail addresses: ware@radiometrics.com (R. Ware), cimini@imaa.cnr.it (D. Cimini), ecampos@anl.gov (E. Campos), graziano.giuliani@aquila.infn.it (G. Giuliani), steve.albers@noaa.gov (S. Albers), m.nelson@radiometrics.com (M. Nelson), steven.koch@noaa.gov (S.E. Koch), paul.joe@ec.gc.ca (P. Joe), stewart.cober@ec.gc.ca (S. Cober).

for upper air monitoring, it is widely recognized that high impact local weather forecasting can be improved using continuous boundary layer thermodynamic measurements (Carbone et al., 2009; Dabberdt et al., 2010; Hoff et al., 2011; Snow et al., 2012; Armstrong et al., 2012).

We present microwave profiler and radiosonde observations by Environment Canada during the 2010 Winter Olympics (Isaac et al., 2012) and numerical gridded analysis provided by the U.S. National Oceanic and Atmospheric Administration. We compare radiometer and six-hour radiosonde thermodynamic soundings during clear, cloudy and precipitating (rain, sleet and snow up to 20 mm/h) conditions. All of the radiometer data are included in the comparison—none were excluded. We also compare radiometer brightness temperature (Tb) observations with brightness temperatures from forward modeled radiosonde soundings and gridded analysis, and neural network, analysis and variational retrieval statistics. This paper extends previous studies of this dataset (Cimini et al., 2011).

2. Instruments and methods

Tropospheric profiles presented in this paper were obtained from a ground-based microwave radiometer profiler (MP), 6-h radiosondes and a numerical weather model gridded analysis. The microwave profiler (Radiometrics MP-3000A) observes 21 K-band (22–30 GHz) and 14 V-band (51–59 GHz) microwave channels at multiple elevation angles, one zenith infrared (9.6–11.5 μm) channel, and surface temperature, humidity and pressure sensors.

The radiometer receives roughly a picowatt of Planck radiation emitted by atmospheric oxygen and water vapor molecules and liquid water, in multiple frequency channels. The atmosphere is semi-transparent in the K-band and lower V-band channels during non precipitating conditions, receiving emission from the atmosphere in addition to cosmic background radiation. The microwave, infrared and surface meteorological observations are automatically converted into continuous temperature, humidity and liquid profiles using radiative transfer equations and neural networks.

2.1. Neural networks

The neural network retrieval method uses historical radiosondes to characterize states of the atmosphere that commonly occur at a particular location. The radiosondes are forward modeled using molecular emission and radiative transfer equations to provide brightness temperatures incident at ground level for each radiosonde sounding. Since radiosonde soundings do not include liquid water (a relatively strong microwave emitter), artificial liquid is included in the radiosonde soundings at levels where humidity is close to saturation (Decker et al., 1978). Four vector neural networks including 26 inputs (8 K-band and 14 V-band microwave channels, an infrared channel, and 3 surface meteorological channels) and 49 hidden nodes generate 58 output nodes (temperature, relative humidity, liquid density and vapor density retrieval heights). Scalar neural networks use the same input and hidden nodes to generate integrated vapor and integrated liquid outputs.

In non-precipitating conditions, neural networks provide temperature and humidity retrievals with accuracy equivalent to observation error typically assigned to radiosonde soundings when they are assimilated into numerical weather models (Kistler et al., 2001; Güldner and Spänkuch, 2001; Cimini et al., 2011). Radiosonde observation error is dominated by representativeness error inherent in characterizing a numerical weather model cell volume by a radiosonde point measurement (Kitchen, 1989), and is roughly an order of magnitude larger than radiosonde point measurement accuracy.

2.2. Zenith and off-zenith retrievals

Thermodynamic and liquid profiles to 10 km height were retrieved from zenith and off-zenith (15° elevation) radiometer observations using neural networks (Solheim et al., 1998). Vertical retrieval intervals are 50 m from the surface to 500 m, 100 m to 2 km, and 250 m to 10 km.

Off-zenith retrievals provide higher accuracy during precipitation by minimizing the affect of liquid water and ice on the radiometer radome. Five years of historical Kelowna, British Columbia (49.93, −119.40, 456 m) radiosondes, adjusted to the radiometer site altitude and to include artificial liquid water profiles, were used for neural network training. The MP was calibrated on December 5, 2009, using liquid nitrogen in a top-mount target. Calibration accuracy of 0.5 K for the top-mount target is verified by Miacci et al., 2013.

2.3. 1DVAR retrievals

One-dimensional variational (1DVAR) methods combining radiometer and numerical weather model gridded analysis outperform other temperature and humidity profiling retrieval methods (Hewison, 2007; Cimini et al., 2010, 2011). 1DVAR combines continuous radiometer observations with satellite and other upper air observations residing in the gridded analysis.

2.4. Radiosondes

Radiosondes (Vaisala RS92-SGP) were launched from the Whistler Valley floor 117 m below and 4.4 km north–northeast of the radiometer to obtain temperature, humidity and wind profiles at 6-h intervals. The Earth System Research Laboratory of the U.S. National Oceanic and Atmospheric Administration (NOAA) provided gridded analysis of Local Analysis and Prediction System (LAPS) temperature, humidity and liquid profiles (Albers et al., 1996). Whistler radiosondes were not included in the LAPS analysis.

Radiometer, radiosonde launch and LAPS analysis grid point locations are indicated in Fig. 1 (adapted from Cimini et al., 2011). Thermodynamic and liquid soundings from the LAPS gridpoint at 700 m altitude were compared with radiometer soundings.

2.5. Other meteorological sensors

The MP and an accompanying suite of meteorological sensors are shown in Fig. 2. Precipitation rate and type,
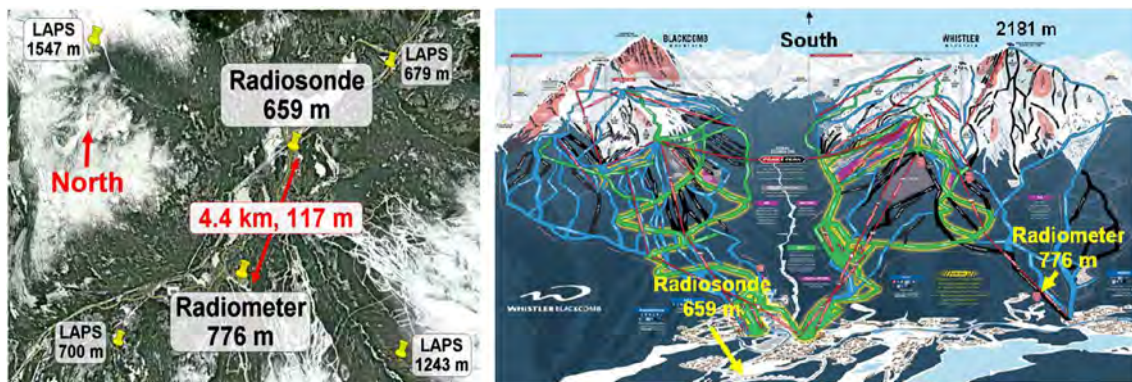
Fig. 1. Radiometer, radiosonde and LAPS grid point locations in the Whistler Valley.

surface temperature and zenith infrared (cloud base temperature) measurements are shown in Fig. 3. A Parsivel laser-based optical particle size and velocity disdrometer measured precipitation type and amount (Battaglia et al., 2010) and precipitation rate was estimated from X-band Doppler radar observations (Sheppard and Joe, 2008). Small differences (<20 K) between surface and cloud base temperatures indicate clouds, whereas large differences (>60 K) indicate no clouds. In general, clouds prevailed 12–17 and 23–28 Feb whereas 18–22 Feb was cloud free. Maximum liquid equivalent precipitation rates approached 20 mm/h with 235-mm total accumulation.

3. Radiometer and radiosonde soundings

Radiometer retrievals (from 15° elevation down valley observations), radiosonde temperature and humidity soundings, radiometer liquid profiles, and radiosonde wind soundings are shown at 6-h radiosonde launch times during a continuous 16-day period in Fig. 4. Strong correlation is evident for the radiometer and radiosonde temperature and humidity soundings up to 10 km height in spite of a 5 °C upper level warm bias in radiometer temperatures (indicated by −58 and −63 °C legend minima to the right of each contour plot). Zenith relative to off-zenith radiometer temperature retrievals (Fig. 5) were inflated during heavy precipitation consistent with emission from accumulated rain, sleet and snow on the upper surface of the radiometer radome.

Also clearly evident in Fig. 4 is close correlation between southwest winds, increases in liquid water and upper level temperature and humidity values in the mid-to-upper troposphere, and the occurrence of precipitation (Fig. 3). This correlation is consistent with up-valley advection of moist maritime air and subsequent liquid condensation with latent heat release (Whistler Valley extends 50 km northeast from Vancouver Sound). Close correlation between radiometer and radiosonde thermodynamic soundings is also reported in warm, moist, convective environments (Ratnam et al., 2013; Sanchez et al., 2013). Lightning forecasting more

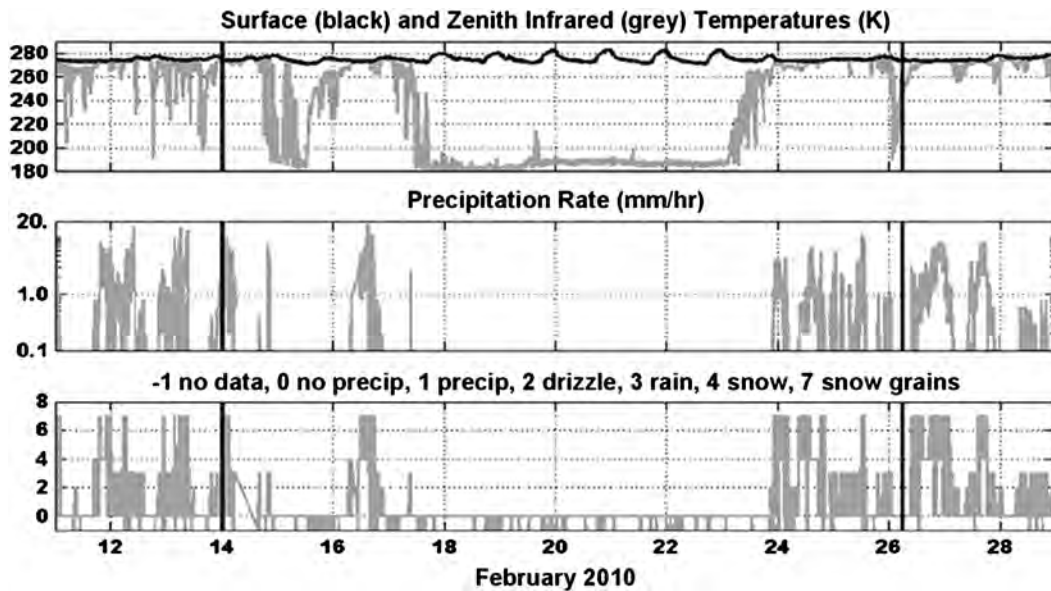**Fig. 2.** Microwave profiler (second from left) and other meteorological sensors.

Fig. 3. Zenith infrared and surface temperature (top), precipitation rate (middle) and precipitation type (bottom) at the radiometer site. Times of rain and no rain profiles shown in Figs. 6–8 are marked by vertical black lines.
Adapted from Cimini et al., 2011

than 2 h in advance based on continuously updated forecast indices generated from MP soundings is reported by Madhulatha et al. (2013).

Differences in boundary layer temperature and relative humidity are evident during clear conditions in the middle section of Fig. 4. For example, more distinct daytime solar heating and elevated nighttime humidity is seen in the radiosonde boundary layer data. This is consistent with different boundary layer conditions for the radiosonde site on the valley floor and the radiometer site 117 m higher on the side of the mountain. In addition, elevated relative humidity near 2 km height is evident for several days in the radiometer data only, consistent with mid-mountain cloud (Harvey's Cloud) that forms when humid valley air is advected up the face of the mountain (Mo et al., 2012).

3.1. Thermodynamic and liquid profiles during precipitation

Zenith radiometer observations during precipitation can be contaminated by microwave emission from liquid water, snow and ice on top of the radiometer radome. Heavy wet snow and sleet, in particular when it is wind-driven, is not easily cleared by a radiometer heater-blower designed to force heated air over the radome. During wind-driven snow and sleet conditions the heated air does not reach upper radome surfaces where maximum ice and snow buildup occurs. The heated air also degrades radiometer surface temperature and humidity measurement accuracy.

Off-zenith observations minimize contamination from ice and snow buildup. For example, Fig. 5 shows zenith and off-zenith temperature retrievals during rain, sleet and snow at near freezing temperatures with precipitation rates approaching 20 mm/h (Fig. 3). Strong degradation is evident in the zenith retrievals whereas the off-zenith retrievals

show no evidence of degradation. Similarly, there is no evidence of degradation in off-zenith humidity and liquid retrievals (not shown).

Example temperature, humidity and liquid profiles are compared in Figs. 6–8 during rain (left panels, 0Z 14 Feb) and no rain (right panels, 6Z 26 Feb). During precipitation the zenith neural network (NNz) temperature retrieval above 500 m height is inflated by emission from accumulated rain, sleet and snow buildup on top of the radiometer radome (Fig. 6, left). Similarly, the NNz vapor density retrieval below 1 km is inflated (Fig. 7, left). In the absence of precipitation, zenith (NNz) and off-zenith (NNs) retrievals are in good agreement (Figs. 6–8, right). In general, off-zenith retrievals are more accurate than zenith retrievals during precipitation (Chan, 2009; Cimini et al., 2011; Raju et al., 2013). Improved vapor density retrieval accuracy is demonstrated in Fig. 7 (right) where a layer of relatively dry air from 2 to 4 km height in the radiosonde sounding is also evident in the 1DVAR retrieval but not in the neural network retrievals.

As shown in Fig. 8, the slant (NNs) compared to zenith (NNz) liquid retrieval shows better agreement with LAPS during rain (left) consistent with emission from accumulated liquid water on top of the radiometer radome during rain. In the absence of rain (but still in the presence of clouds), liquid density from the analysis and estimated from a radiosonde (Decker et al., 1978) shows similar peak values near 0.16 g/m³ and 2 km height whereas 0.03 g/m³ peak near 2 km height was observed by the radiometer. Considering that the radiometer field-of-view near 2 km height is roughly 1% of the 10-km analysis grid spacing and that the radiosonde liquid is a rough estimate, large liquid density differences between the three methods are not surprising. However, the 1DVAR liquid retrieval shows zero liquid, indicating that the 1DVAR
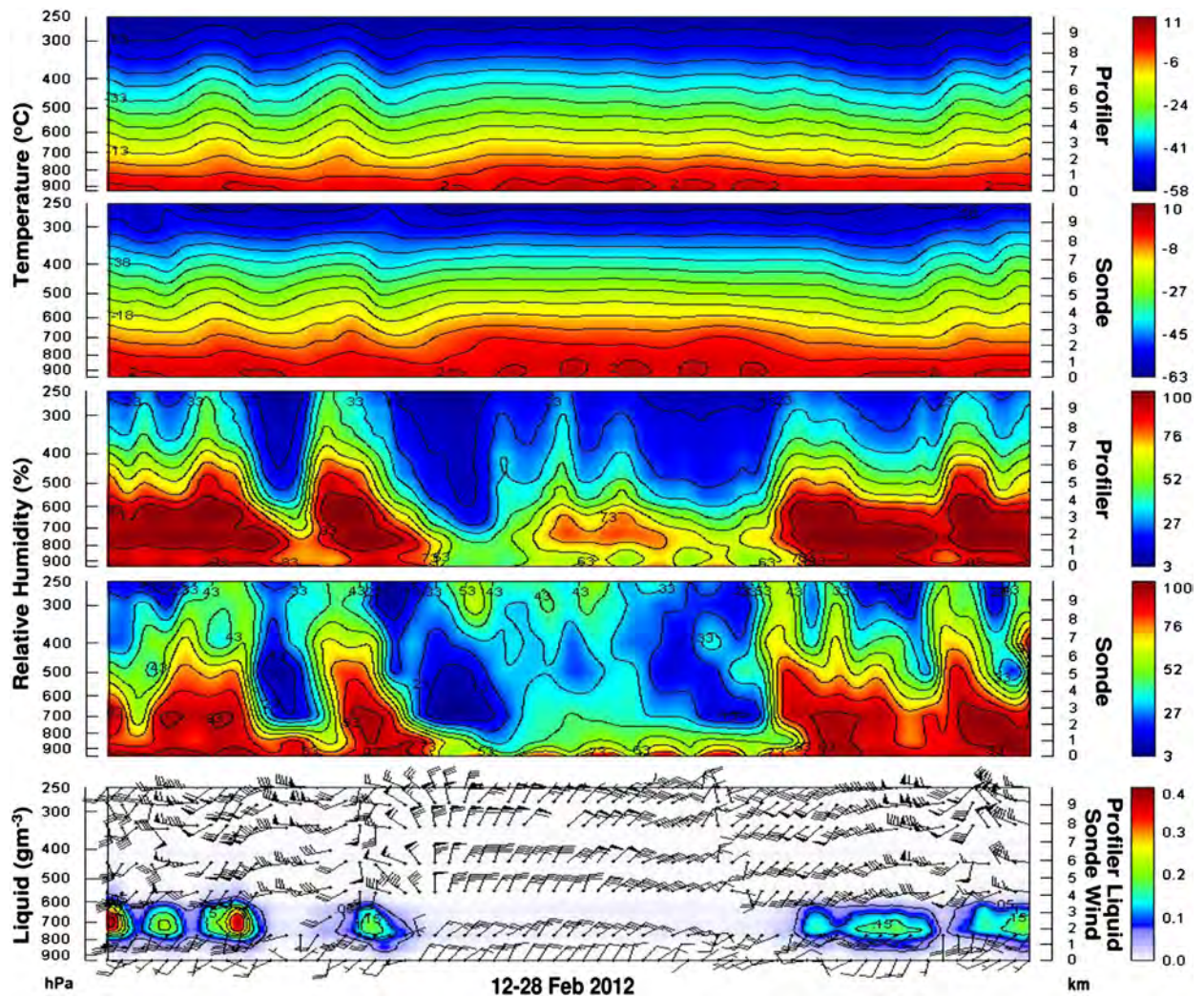
Fig. 4. Radiometer neural network (temperature, humidity and liquid) and radiosonde (temperature, humidity and wind) soundings.

liquid retrieval method would benefit from further development. In particular, balloon-borne liquid sensors (Serke et al., 2013) provide independent liquid profile measurements that can be used to validate and potentially improve 1DVAR liquid retrievals.

3.2. Liquid water retrievals

Integrated liquid water retrieval from microwave radiometer observations near the 22.2 GHz water vapor molecular resonance is well established (e.g. Westwater, 1978; Turner et al., 2007). It is also well established that microwave measurements alone are relatively insensitive to vertical liquid water distribution (Crewell et al., 2009). However, infrared cloud base temperature measurements and saturated humidity height distribution climatology (from historical radiosondes) contain additional liquid profile information.

The neural network makes use of integrated liquid water (from microwave), cloud base temperature and height (from infrared and microwave) and liquid profile climatology (from historical radiosondes) in liquid profile retrievals (e.g. Figs. 4 and 8; Ware et al., 2003; Knupp et al., 2009; Madonna et al., 2009; Madhulatha et al., 2013). Neural network liquid profile retrieval accuracy of 50% has been determined by comparison with balloon-borne supercooled liquid sensors (Ware et al., 2003; Serke et al., 2013). Differences between fixed volume radiometric observations and balloon-borne liquid sensor point measurements along an uncontrolled flight path contribute to the large uncertainty. An alternative method combining microwave radiometer and cloud radar measurements obtains 60% or larger liquid profile retrieval uncertainty (Ebell et al., 2010).

3.3. Thermodynamic retrieval accuracy

Statistical comparisons of analysis, neural network and variational profiles with radiosondes including mean deviation (MD), standard deviation (STD) and root mean square (RMS) during the 16-day study period are shown in Figs. 9 and 10 for temperature and relative humidity, respectively.
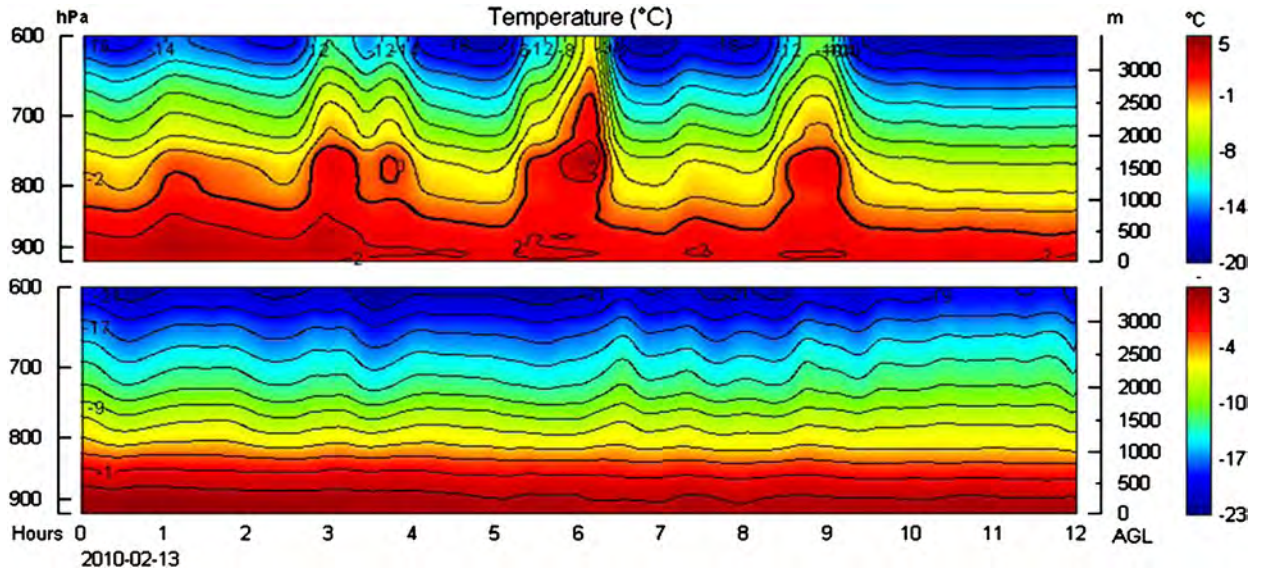
Fig. 5. Zenith (NNz, top) and off-zenith (NNs, bottom) retrievals to 3500 m height.

Neural network temperature retrieval errors below 800 m height (Fig. 9) are smaller than the observation error assigned to radiosondes when they are assimilated in numerical weather models (Cimini et al., 2011), consistent with radiometer-tower temperature accuracy at lower levels reported by Friedrich et al. (2012). Above 800 m height, errors are up to three times larger than long-term statistical errors reported during non-precipitating conditions (Güldner and Spänkuch, 2001; Liljegren et al., 2004; World Meteorological Organization, 2008). We attribute the relatively large standard deviation for zenith and slant neural network retrievals above 800 m to decreasing microwave sensitivity with height; zenith retrieval accuracy is also

degraded by emission from accumulated rain, sleet and snow on top of the radiometer radome (e.g. Fig. 6, left). Accurate performance of off-zenith neural network retrievals during heavy precipitation is reported by Chan (2009), Cimini et al. (2011) and Raju et al. (2013).

As seen in Figs. 9 and 10, errors are smaller for off-zenith neural net 'slant' (NNs) retrievals. Overall, neural network retrievals up to 800 m height and 1DVAR retrievals up to 10 km height show better accuracy during all weather conditions than the observation error typically assigned to radiosonde data when they are assimilated into numerical weather models (Kitchen, 1989; Kistler et al., 2001).
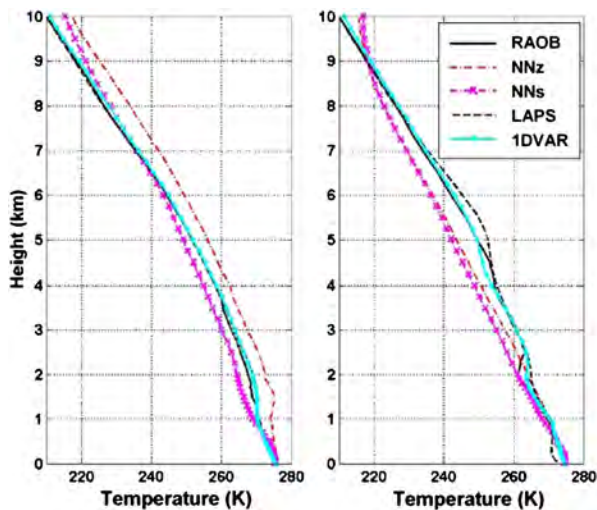

Fig. 6. Radiosonde (RAOB), neural network zenith (NNz) and 15° elevation 'slant' (NNs), gridded analysis (LAPS) and one-dimensional variational (1DVAR) temperature profiles during rain (left) and no rain (right). Adapted from Cimini et al., 2011
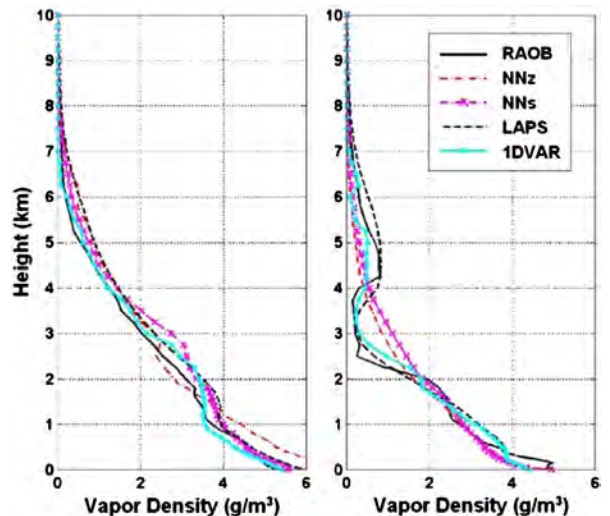

Fig. 7. Same as Fig. 6 for vapor density profiles. Adapted from Cimini et al., 2011
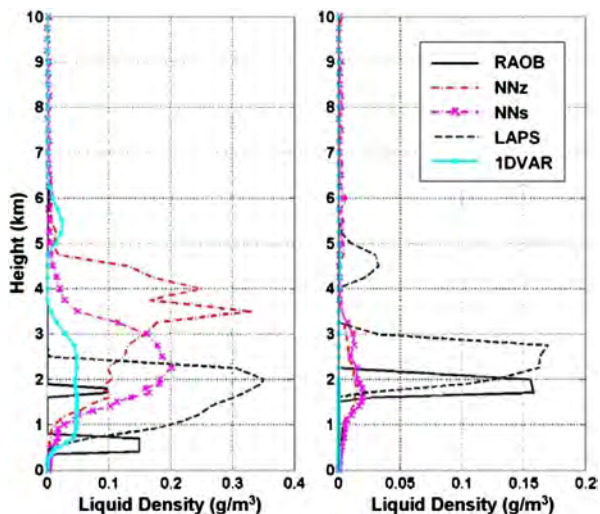
Fig. 8. Same as Fig. 6 for liquid density profiles.
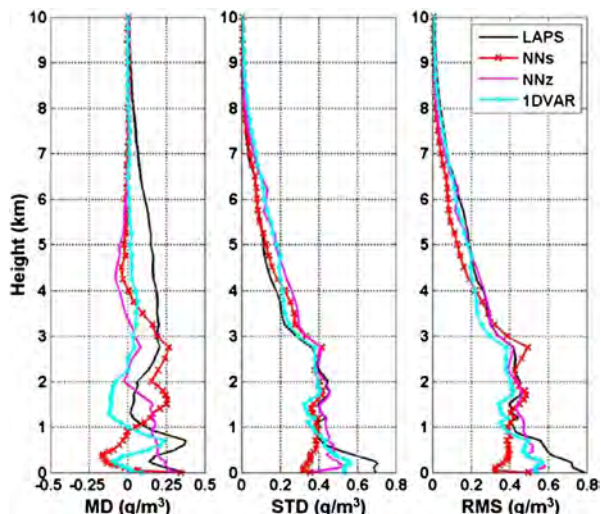Adapted from Cimini et al., 2011

Fig. 10. Same as Fig. 9 for humidity.
Adapted from Cimini et al., 2011

4. Brightness temperatures

Brightness temperature time series observed by the radiometer and simulated from radiosondes and LAPS analysis at 22.234, 30, 51.248, and 58.8 GHz (K-band channels 2 and 21, V-band channels 1 and 14) are shown in Figs. 10–13; scatter plots are shown in Figs. 14–17. Observed and simulated brightness temperatures in the K-band are attributed primarily to emission from water vapor and liquid, and to emission from oxygen and liquid in the V-band (Westwater et al., 2005). The water vapor emission spectrum is centered at 22.234 GHz (K2) and is pressure broadened, whereas liquid water emission is roughly proportional to the frequency squared. Emission from the water vapor continuum also contributes to K and V-band brightness temperatures (Payne et al., 2011).
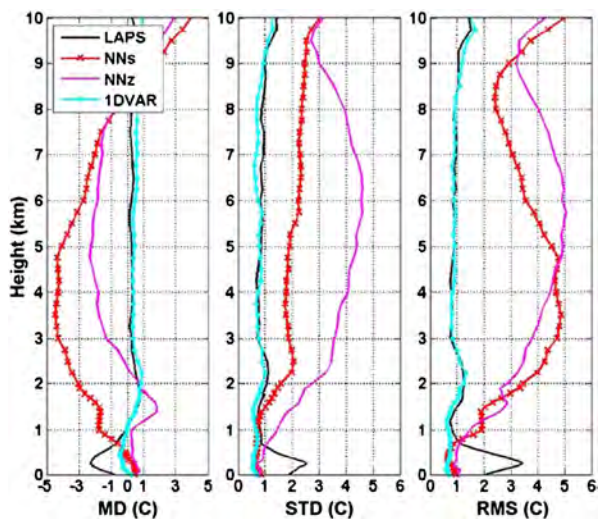

Fig. 9. Statistics of analysis (LAPS), neural network (NNz, NNs) and 1DVAR temperature profiles compared with radiosondes.
Adapted from Cimini et al., 2011

4.1. K-band (22–30 GHz)

In the lowest observed K-band channel (22.234 GHz, K2), observed and simulated brightness temperatures are similar (Fig. 11). In general, radiometer and LAPS analysis brightness temperatures show good agreement, with higher variability in the radiometer data as strongly emitting cloud, rain and mixed-phase liquid drifts into the radiometer field-of-view. Two values of radiosonde brightness temperatures are shown during cloudy conditions, the lower value assuming no liquid and the higher value assuming modeled liquid (Decker et al., 1978). Roughly 60 K average and 20 K brightness temperature peak to peak variability is seen in Fig. 11 during clear conditions (17–23 Feb), dominated by water vapor emission.

In the highest observed K-band channel (30 GHz, K21), roughly 40 K average and 5 K brightness temperature peak to peak variability is seen during 17–23 February clear conditions (Fig. 12). Brightness temperatures observed in this channel are dominated by water vapor continuum emission.

4.2. V-band (51–59 GHz)

In the lowest observed V-band channel (51.248 GHz, V1), brightness temperatures are similar to K-band with high variability due to cloud and other liquid in the radiometer field of view. However, emissions from oxygen molecular resonances near 60 GHz also contribute, and are dominant during clear conditions. Diurnal temperature signatures are evident during clear conditions in the brightness temperature time series in Fig. 13. The water vapor continuum also contributes to lower V-band brightness temperatures.

In the highest V-band channel (58.8 GHz, V14), the radiometer is sensitive to temperature, with an effective range of approximately 300 m (1/e energy received from <300 m distance). At 15° elevation the 300 m effective range corresponds to an effective height of approximately 75 m (1/e energy received from <75 m height). Brightness temperature
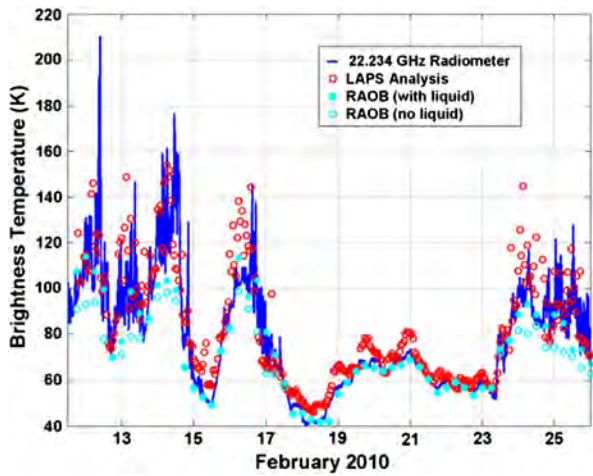
Fig. 11. Observed and simulated 22.234 GHz brightness temperatures at 15° elevation.
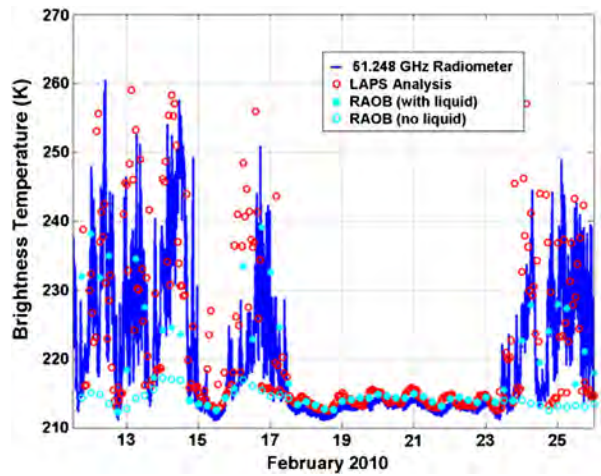

Fig. 13. Same as Fig. 11 for 51.248 GHz.

observed in this channel at 15° elevation is a direct measurement of the average physical air temperature within the radiometer field of view, falling off exponentially to 1/e at 75 m height (300 m distance). Relatively good agreement is seen between radiometer, analysis and radiosonde brightness temperatures during cloudy conditions, and between radiometer and radiosonde temperatures in all weather conditions. However, during clear (17–23 Feb) nighttime conditions, the analysis shows as much as 5 K cold bias. This clear air bias would be reduced or eliminated if local surface temperature data were included in the LAPS analysis.

4.3. Scatter plots

Analysis and radiosonde brightness temperature simulations are compared to radiometer observations in Figs. 15–18 during all weather conditions at 22.234 (K2), 30 (K21), 51.248 (V1) and 58.8 (V14) GHz, the lowest (K2, V1) and highest (K21, V14) observed K and V-band channels. Clear conditions are indicated by radiometer zenith infrared temperatures <200 K.

At 22.234 GHz (K2), clear sky LAPS and RAOB show 6.0 and 2.4 K rms agreement with radiometer brightness temperatures (Fig. 15) dominated by large positive outliers that occur when zenith infrared temperature indicates clear skies and the LAPS analysis includes liquid.

At 30 GHz (K21), clear sky LAPS and RAOB show 3.4 and 3.1 K rms agreement with radiometer brightness temperatures. Large positive outliers occur when the radiometer indicates clear skies and liquid is present in the LAPS analysis.

At 51.248 GHz (V1) during all weather conditions, LAPS scatter is relatively large, and clear LAPS brightness temperatures are relatively cold (Fig. 17). During clear conditions, LAPS and RAOB show reasonable (2.0 and 1.0 K rms) agreement with radiometer brightness temperatures. Up to 4 K positive bias is seen when clear skies are observed by the radiometer and liquid is present in the LAPS analysis.
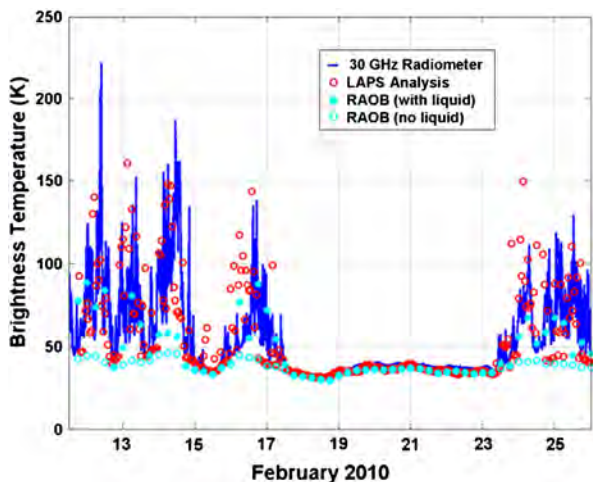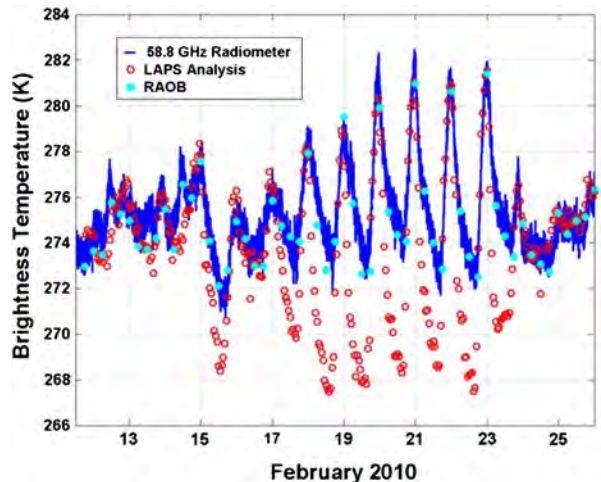

Fig. 12. Same as Fig. 11 for 30 GHz.

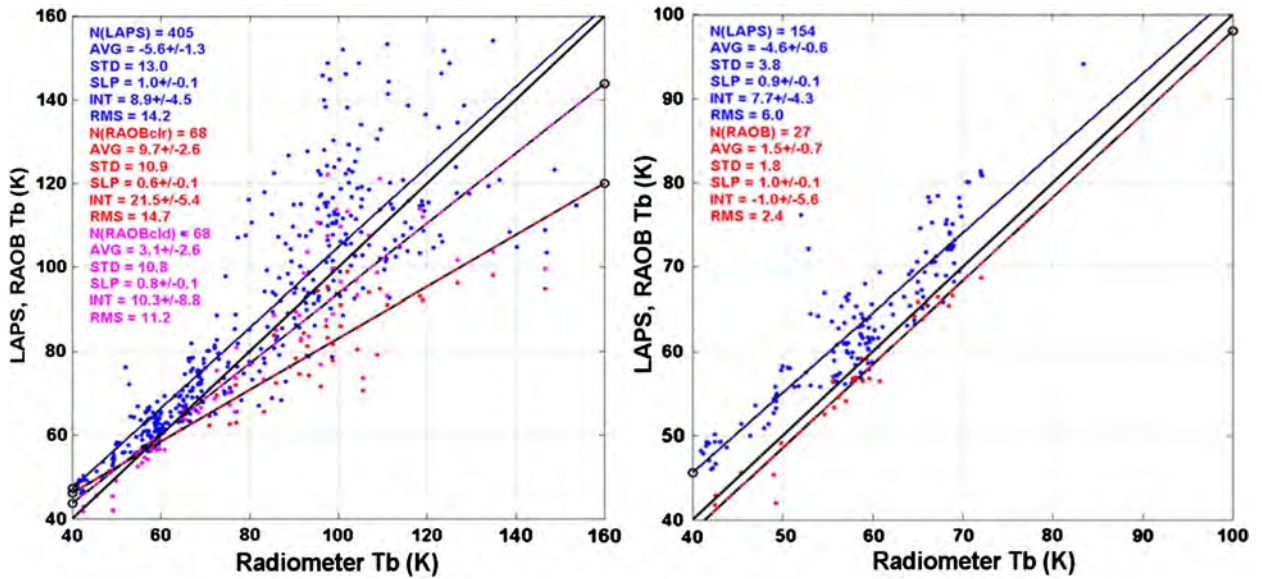**Fig. 14.** Same as Fig. 11 for 58.8 GHz.

Fig. 15. Simulated (LAPS, RAOB) vs. observed (radiometer) 22.234 GHz brightness temperatures during all weather (left) and clear (right) conditions; radiosonde (red: no liquid; magenta: simulated liquid), number of elements (N), mean observation-simulation difference (AVG), standard deviation (STD), slope (SLP) and intercept (INT) of linear fit, and root-mean-square (RMS). (For interpretation of the references to color in this figure legend, the reader is referred to the web version of this article.)

At 58.8 GHz (V14), LAPS agreement is better during all weather compared to clear conditions, since liquid water and ambient air brightness temperatures are similar for the 75 m effective height observed at 15° elevation (Fig. 18). In clear conditions, LAPS and RAOB show 4.0 and 0.9 K rms agreement with radiometer brightness temperatures. Larger errors for LAPS are consistent with cold bias evident in Fig. 14 during clear night time conditions.

Much larger variability is seen in the analysis and radiosonde simulated brightness temperatures during all weather compared to clear conditions due to relatively strong emission from liquid water and large differences in spatial resolution of the LAPS analysis (10 km), radiometer (<6° beamwidth) and radiosonde (point) measurements. Simulated radiosonde brightness temperatures are compared statistically with the 22 radiometer-observed microwave channels in Table 1.
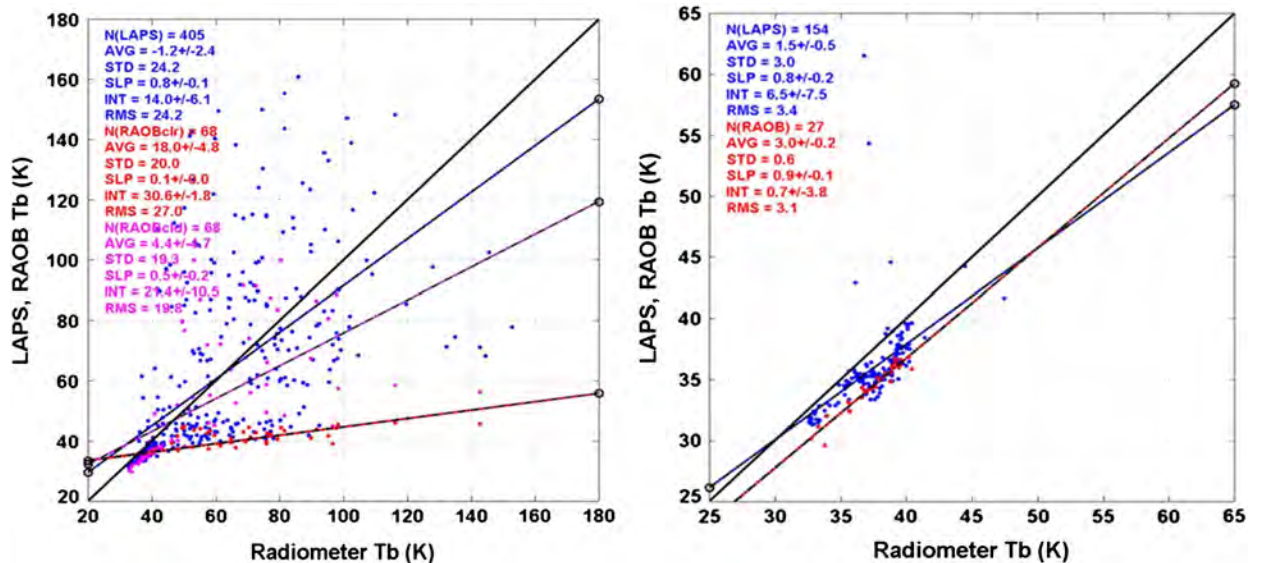

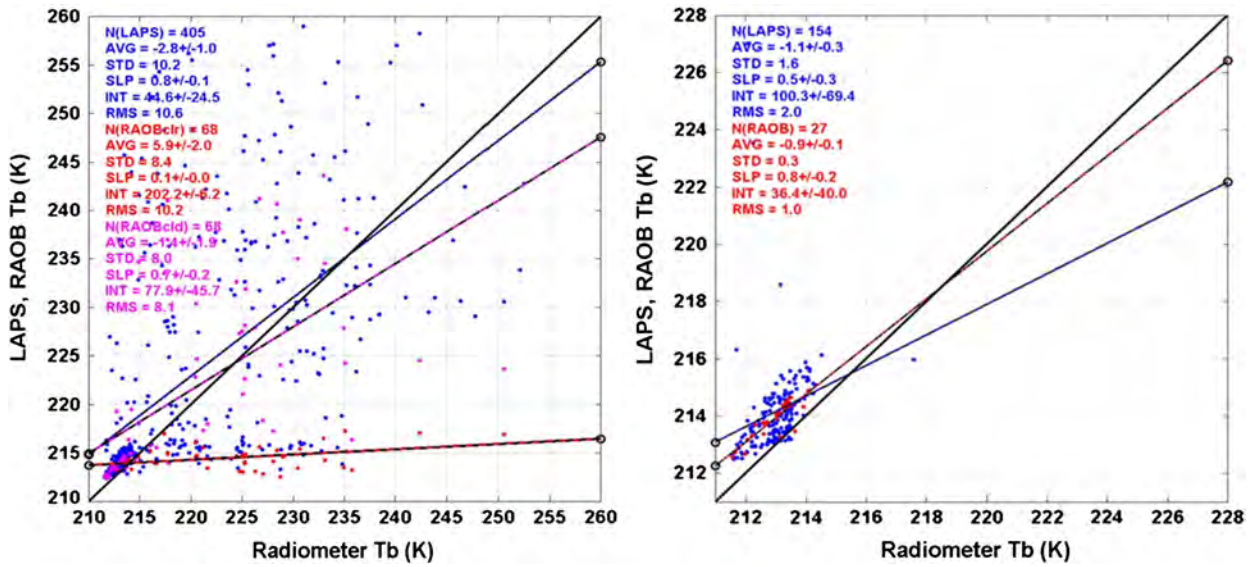**Fig. 16.** Same as Fig. 15 for 30 GHz.

Fig. 17. Same as Fig. 15 for 51.248 GHz.

4.4. Brightness temperature statistics

Clear sky off-zenith radiometer minus radiosonde brightness temperature statistics are listed in Table 1. Average (bias) for the K-band is positive and ranges between 1.5 and 3 K consistent with radiosonde dry bias (Turner et al., 2003; Cady-Pereria et al., 2008; Miloshevich et al., 2009). For the lowest four V-band channels, 1–2 K negative bias is consistent with small (roughly 0.1° leveling error) and with negative temperature retrieval bias in Fig. 9. Standard deviations are relatively small, less than 1.9 and 0.7 K for K and V bands and rms is less than 3.2 and 2.0 K. Higher K-band variability (STD <1.3 K, RMS <2.8 K) compared to V-band

(STD <0.05 K, RMS <0.9 K) is consistent with greater spatial variability of humidity relative to temperature. Correlation coefficients (COR) and slope (SLP) are in relatively good agreement (>0.95 K, 0.9–1.06 K) except for channel 22 (0.88 K, 0.83 K) due to a small number of outliers (Fig. 16, right). Intercepts (INT) for channels 2–21 lie within the range −8 to +3 K and channel 22 INT is 36.41 K (due to outliers). For channels 27–35 the intercepts decrease nearly monotonically from −0.45 to −18.22 K. The average standard error (SDE) for all channels is 0.74 K.

In general, Table 1 statistics demonstrate good agreement between observed (radiometer) and simulated (radiosonde) brightness temperatures, consistent with 0.5 K radiometer
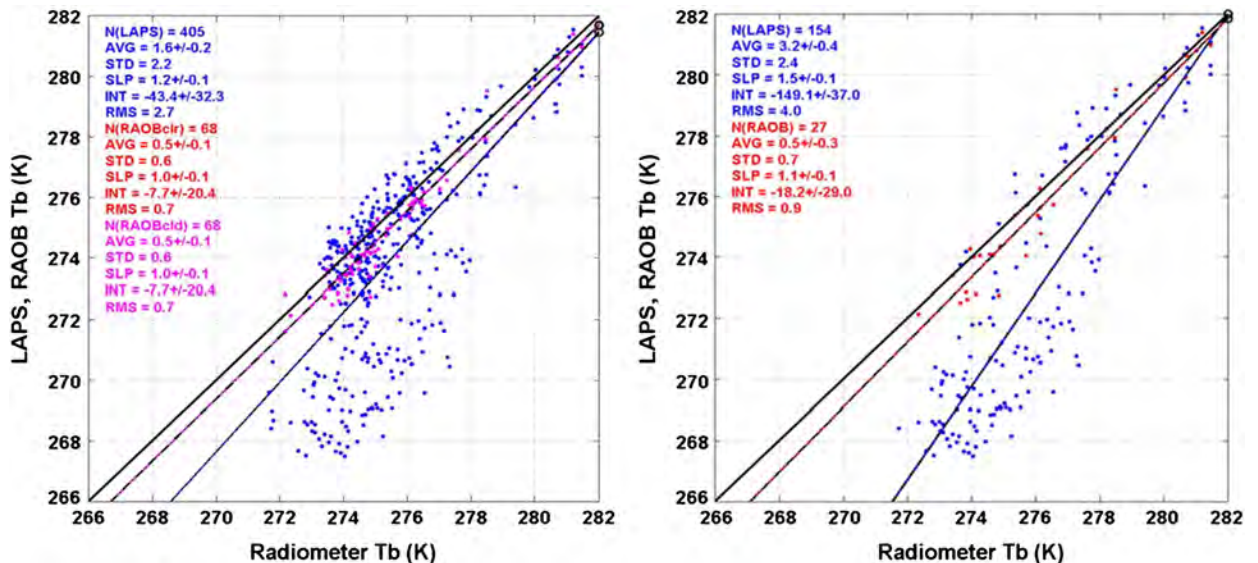

Fig. 18. Same as Fig. 15 for 58.8 GHz.

Table 1

Clear-sky radiometer observations minus radiosonde simulated brightness temperature statistics including channel number, frequency (GHz), number of elements (N), mean difference (AVG), standard deviation (STD), root-mean-square (RMS), correlation coefficient (COR), slope (SLP) and intercept (INT) of linear fit, and standard error (SDE).

Chan#	Freq	N	AVG	STD	RMS	COR	SLP	INT	SDE
2	22.234	27	1.55	1.83	2.42	0.97	0.99	−1.04	1.87
3	22.500	27	1.86	1.84	2.65	0.97	1.00	−1.65	1.88
5	23.034	27	2.18	1.71	2.81	0.97	1.00	−1.94	1.75
7	23.834	27	2.90	1.35	3.25	0.98	0.99	−2.29	1.38
10	25.000	27	1.97	0.95	2.22	0.98	0.96	−0.40	0.95
13	26.234	27	2.59	0.78	2.75	0.97	0.93	0.06	0.76
17	28.000	27	2.97	0.68	3.10	0.97	0.90	0.85	0.63
21	30.000	27	3.00	0.58	3.11	0.96	0.90	0.72	0.55
22	51.248	27	−0.93	0.34	1.00	0.88	0.83	36.41	0.32
23	51.760	27	−1.37	0.25	1.42	0.95	1.04	−6.98	0.25
24	52.280	27	−1.90	0.22	1.94	0.98	1.03	−4.54	0.23
25	52.804	27	−1.14	0.28	1.20	0.98	1.03	−5.74	0.29
26	53.336	27	−0.17	0.35	0.39	0.98	0.99	2.35	0.35
27	53.848	27	0.00	0.40	0.40	0.98	1.00	−0.48	0.40
28	54.400	27	0.41	0.42	0.59	0.98	1.02	−5.54	0.42
29	54.940	27	0.46	0.47	0.67	0.98	1.03	−7.57	0.48
30	55.500	27	0.53	0.51	0.74	0.98	1.03	−10.15	0.52
31	56.020	27	0.53	0.56	0.78	0.98	1.04	−11.81	0.56
32	56.660	27	0.40	0.61	0.73	0.98	1.05	−13.49	0.61
33	57.288	27	0.50	0.64	0.82	0.97	1.06	−16.44	0.63
34	57.964	27	0.28	0.68	0.74	0.97	1.06	−16.22	0.68
35	58.800	27	0.52	0.68	0.86	0.97	1.06	−18.22	0.67
Average:			0.78	0.73	1.57	0.97	1.00	−3.82	0.74

calibration accuracy (Miacci et al., 2013), horizontal (4.4 km) and altitude (117 m) differences between radiometer and radiosonde sites, radiosonde dry bias and small radiometer leveling error.

5. Discussion

Radiosonde and off-zenith radiometer temperature and humidity retrievals show close correlation up to 10 km height in all weather conditions. Correlation below 1 km is also strong in spite of 4 km separation and 120 m altitude difference between the radiometer and radiosonde launch sites. In addition, southwest winds are correlated with liquid water and inflated upper level temperature and relative humidity values, consistent with liquid condensation and latent heat release associated with ascending moist maritime air.

Comparison with radiosondes shows that zenith and off-zenith radiometer retrieval accuracy below 800 m height, and variational retrievals up to 10 km height, are better than the observation error typically assigned to radiosonde soundings when they are assimilated into numerical weather models. Radiometer retrieval accuracy above 800 m height is up to three times larger than previously reported in non-precipitating conditions. Relatively large standard deviation of zenith radiometer retrievals during precipitation is attributed to emission from accumulated rain, sleet and snow on top of the radiometer radome. Standard deviation for off-zenith retrievals is less than half of that for zenith retrievals up to 7 km height (Fig. 9). In contrast, maximum off-zenith bias is twice as large as zenith bias, attributed to small radiometer leveling error.

Time series and scatter plots of observed and simulated brightness temperatures show good agreement except in upper V-band channels with high sensitivity to boundary layer temperatures. For the upper V-band, up to 5 K cold bias in simulated analysis brightness temperatures is seen, compared to radiometer observations and simulated radiosondes during clear, nocturnal conditions.

Although the results reported here pertain to winter conditions only, radiosonde-equivalent observation accuracy and forecast improvements are also reported in warm, moist, convective environments (Madhulatha et al., 2013; Ratnam et al., 2013).

6. Conclusions

It is widely recognized that boundary layer thermodynamic soundings with adequate space-time resolution are needed to improve local weather forecasting. Radiosonde-equivalent observation accuracy is demonstrated for boundary layer radiometer neural network thermodynamic retrievals during weather conditions including rain, sleet and snow. Similar accuracy is demonstrated for variational retrievals combining radiometer soundings and gridded analysis up to 10 km height; close correlation is evident between radiometer neural network and radiosonde thermodynamic soundings to similar height. Liquid profiling is demonstrated based on microwave, infrared and surface meteorological measurements combined via neural network with liquid vertical distribution information in historical radiosonde soundings. Close correlation is seen between wind direction, liquid water and tropospheric thermodynamic profiles. These results demonstrate that a microwave profiler can provide continuous thermodynamic soundings with radiosonde-like accuracy in all weather

conditions. This capability has strong potential to improve high impact local weather forecasting by making continuously updated stability indices readily available and by providing essential data for accurate numerical weather prediction.

Glossary and acronyms

Tb	brightness temperature
K-band	22–30 GHz
V-band	51–59 GHz
LAPS	local analysis and prediction system
1DVAR	a one-dimensional variational method combining radiometer and numerical weather model gridded analysis
NN	neural network
NNz	zenith neural network retrievals from zenith observations
NNs	off-zenith 'slant' neural network retrievals from 15° elevation observations
K1–K21	K-band radiometer channels
V1–V14	V-band radiometer channels

Acknowledgments

Disclosure

Some of the data presented in this article were observed by a microwave profiler manufactured by Radiometrics. The first author is a founder of Radiometrics where he serves as Chief Scientist.

References

Albers, S., McGinley, J., Birkenheuer, D., Smart, J., 1996. The Local Analysis and Prediction System (LAPS): Analyses of Clouds, Precipitation, and Temperature, Weather and Forecasting.

Armstrong, J., Doye, J., Emch, P., Gail, W., Gochis, D., Gruntfest, E., Hartmann, H., Kloesel, K., Lampson, N., Madden, J., McBean, G., McLaughlin, D., Raftery, A., Rasmussen, J., Smith, P., Toohey-Morales, J., 2012. Weather Services for the Nation: Becoming Second to None. U.S. National Academy of Sciences.

Battaglia, A., Rustemeier, E., Tokay, A., Blahak, U., Simmer, C., 2010. PARSIVEL snow observations: a critical assessment. J. Atmos. Ocean. Technol. 27, 333–344.

Cady-Pereira, K., Shephard, M., Turner, D., Mlawer, E., Clough, S., 2008. Improved Daytime Column-Integrated Precipitable Water Vapor from Vaisala Radiosonde Humidity Sensors, JAOT.

Carbone, R., Block, J., Boselly, S., Carmichael, G., Carr, F., Chandrasekar, V., Gruntfest, E., Hoff, R., Krajewski, W., Lemone, M., Purdom, J., Schlatter, T., Takle, E., Titlow, J., Marshall, C., 2009. Observing Weather and Climate from the Ground up, a Nationwide Network of Networks. U.S. National Academy of Sciences.

Chan, P.W., 2009. Performance and Application of a Multi-wavelength, Ground-based Microwave Radiometer in Intense Convective Weather. Met. Zeit.

Cimini, D., Westwater, E., Gasiewski, A., 2010. Temperature and humidity profiling in the Arctic using ground-based millimeter-wave radiometry and 1DVAR. IEEE Trans. Geosci. Remote Sens. 4959–4969.

Cimini, D., Campos, E., Ware, R., Albers, S., Giuliani, G., Oreamuno, J., Joe, P., Koch, S., Cober, S., Westwater, E., 2011. Thermodynamic atmospheric profiling during the 2010 Winter Olympics using ground-based microwave radiometry. IEEE Trans. Geosci. Remote Sens. 47, 3098–3106.

Crewell, S., Ebell, K., Loehnert, U., Turner, D., 2009. Can liquid water profiles be retrieved from passive microwave zenith observations? Geophys. Res. Lett. 36.

Dabberdt, W., Carbone, R., Chen, S., Forbes, G., Foufoula-Giorgiou, E., Morss, R., Snow, J., Zeng, X., 2010. When Weather Matters: Science and Service to Meet Critical Societal Needs. U.S. National Academy of Sciences.

Decker, M., Westwater, E., Guiraud, F., 1978. Experimental evaluation of ground-based microwave sensing of atmospheric temperature and water vapor. J. Appl. Meteorol. 17, 1788–1795.

Ebell, K., Loehnert, U., Crewell, S., Turner, D., 2010. On characterizing the error in a remotely sensed liquid water content profile. Atmos. Res. 98, 57–68.

Friedrich, K., Lundquist, J., Aitken, M., Kalina, E., Marshall, R., 2012. Stability and Turbulence in the Atmospheric Boundary Layer: an Intercomparison of Remote Sensing and Tower Observations. GRL 39, 1–6.

Güldner, J., Spänkuch, D., 2001. Remote sensing of the thermodynamic state of the atmospheric boundary layer by ground-based microwave radiometry. J. Atmos. Ocean. Technol. 825–933.

Hewison, T., 2007. 1D-VAR retrievals of temperature and humidity profiles from a ground-based microwave radiometer. IEEE Trans. Geosci. Remote Sens. 45, 2163–2168.

Hoff, R., Hardesty, R., Carr, F., Weckwerth, T., Koch, S., Benedetti, A., Crewell, S., Cimini, D., Turner, D., Feltz, W., Demoz, B., Wulfmeyer, V., Sisterson, D., Ackerman, T., Fabry, F., Knupp, K., Carbone, R., Serafin, R., 2011. Thermodynamic Profiling Technologies Workshop, NSF-NWS Workshop Report.

Isaac, G., Joe, P., Mailhot, J., Bailey, M., Belair, S., Boudala, F., Brugman, M., Campos, E., Carpenter, R., Crawford, R., Cober, S., Denis, B., Doyle, C., Reeves, H., Gultepe, I., Haiden, T., Heckman, I., Huang, L., Milbrandt, J., Mo, R., Rasmussen, R., Smith, T., Stewart, R., Wand, D., Wilson, J., 2012. Science of nowcasting olympic weather for Vancouver 2010 (SNOW-V10): a world weather research programme project. Pure Appl. Geophys.

Kistler, R., Kalnay, E., Collins, W., Saha, S., White, G., Woolen, J., Chelliah, M., Ebiszusaki, W., Kanamitsu, M., Kousky, V., van den Dool, H., Jenne, R., Fiorino, M., 2001. The NCEP-NCAR 50 Year Reanalysis, BAMS. 247–267.

Kitchen, M., 1989. Representativeness Errors for Radiosonde Observations (QJRMS).

Knupp, K., Ware, R., Cimini, D., Vandenberghe, F., Vivekanandan, J., Westwater, E., Coleman, T., 2009. Ground-based passive microwave profiling during dynamic weather conditions. J. Atmos. Ocean. Technol. 1057–1073.

Liljegren, J., Boukabara, S., Cady-Pereira, K., Clough, S., 2004. The Effect of the Half-Width of the 22-GHz Water Vapor Line on Retrievals of Temperature and Water Vapor Profiles with a Twelve-Channel Microwave Radiometer, TGARS.

Madhulatha, A., Rajeevan, M., Venkat Ratnam, M., Bhate, Jyoti, Naidu, C.V., 2013. Nowcasting severe convective activity over South-east India using ground-based microwave radiometer observations. J. Geophys. Res.

Madonna, F., Russo, F., Dutton, E., Ware, R., Pappalardo, G., 2009. Mid-Tropospheric Supercooled Liquid Water Observed by a Microwave Profiler, GRL, 2009.

Maschwitz, G., Loehnert, U., Crewell, S., Rose, T., Turner, D., 2013. Investigation of ground-based microwave radiometer calibration techniques at 530 hPa. Atmos. Meas. Tech. (in discussion).

Miacci, M., Angelis, C., Calheiros, A., Machado, L., 2013. Some considerations on the cryogenic calibration technique for microwave and millimeter wave ground-based radiometry. IEEE Trans. Geosci. Remote Sens. (in review).

Miloshevich, L., Vömel, H., Whiteman, D., Leblanc, T., 2009. Accuracy Assessment and Correction of Vaisala RS92 Radiosonde Water Vapor Measurements, JGR.

Mo, R., Joe, P., Isaac, G., Gultepe, I., Rasmussen, R., Milbrandt, J., McTaggart-Cowan, R., Mailhot, J., Brugman, M., Smith, T., Scott, B., 2012. Mid-mountain clouds at whistler during the Vancouver 2010 Winter Olympics and Paralympics, pure and applied geophysics.

Payne, V., Mlawer, E., Cady-Pereira, K., Moncet, J., 2011. Water vapor continuum absorption in the microwave. IEEE Trans. Geosci. Remote Sens. 49, 2194–2208.

Raju, S., Renju, R., Antony, T., Mathew, N., Moorthy, K., 2013. Microwave radiometric observation of a waterspout over coastal Arabian Sea. IEEE Geosci. Remote. Sens. Lett.

Ratnam, M., Durga Santhi, Y., Rajeevan, M., Vijaya Bhaskara Rao, S., 2013. Diurnal variability of stability indices observed using radiosonde observations over a tropical station: Comparison with microwave radiometer measurements. Atmos. Res. 124, 21–33.

Sánchez, J., Posada, R., García-Ortega, E., López, L., Marcos, J., 2013. A method to improve the accuracy of continuous measuring of vertical profiles of temperature and water vapor density by means of a ground-based microwave radiometer. Atmos. Res. 122, 43–54.

Serke, D., Hall, E., Bognar, J., Jordan, A., Abdo, S., Bake, K., Seite, T., Nelson, M., Reehorst, A., Ware, R., McDonough, F., Politovich, M., 2013. Supercooled liquid water content profiling with a new vibrating wire sonde compared to a ground-based microwave radiometer. J. Atmos. Oceanic Technol. (in review)

Sheppard, B., Joe, P., 2008. Performance of the precipitation occurrence sensor system as a precipitation gauge. J. Atmos. Ocean. Technol. 25, 196–212.

Snow, J., Zeng, X., Klein, P., Sarnat, S., Shepherd, J., Stanley, E., 2012. Urban Meteorology: Forecasting, Monitoring, and Meeting Users' Needs, U.S. National Academy of Sciences.

Solheim, F., Godwin, J., Westwater, E., Han, Y., Keihm, S., Marsh, K., Ware, R., 1998. Radiometric profiling of temperature, water vapor, and cloud liquid water using various inversion methods. Radio Sci. 33, 393–404.

Turner, D., Lesht, B., Clough, A., Liljegren, J., Revercomb, H., Tobin, D., 2003. Dry Bias and Variability in Vaisala RS80-H Radiosondes: The ARM Experience, JAOT.

Turner, D., Clough, S., Liljegren, J., Clothiaux, E., Cady-Pereira, K., Gaustad, K., 2007. Retrieving Liquid Water Path and Precipitable Water Vapor From the Atmospheric Radiation Measurement (ARM) Microwave Radiometers, TGRS.

Ware, R., Solheim, F., Carpenter, R., Güldner, J., Liljegren, J., Nehrkorn, T., Vandenberghe, F., 2003. A multi-channel radiometric profiler of temperature, humidity and cloud liquid. Radio Sci. 44.1–44.13.

Westwater, E., 1978. The accuracy of water vapor and cloud liquid determinations by dual-frequency ground-based microwave radiometry. Radio Sci. 13, 677–685.

Westwater, E., Crewell, S., Mäztler, C., Cimini, D., 2005. Principles of Surface-based Microwave and Millimeter wave Radiometric Remote Sensing of the Troposphere, Quaderni Soc. Ital. Elettromag.

World Meteorological Organization, 2008. Guide to Meteorological Instruments and Methods of Observation, Seventh edition. (WMO-No. 8).